Jin, M., Zuo, W., and Chen, Q. 2012. "Improvements of fast fluid dynamics for simulating airflow in buildings," *Numerical Heat Transfer, Part B: Fundamentals*, 62(6), 419-438.

Improvements of Fast Fluid Dynamics for Simulating Airflow in Buildings

Mingang Jin[1], Wangda Zuo[2], Qingyan Chen[1]

[1]*School of Mechanical Engineering, Purdue University, West Lafayette, IN 47906, USA*
[2]*Environmental Energy Technologies Division, Lawrence Berkeley National Laboratory, Berkeley, CA 94720, USA*

Qingyan Chen (Corresponding Author)
Email: yanchen@purdue.edu
Phone: +1-765-496-7562
Fax: +1-765-494-0539

Abstract

Fast Fluid Dynamics (FFD) could be potentially used for real-time indoor airflow simulations. This study developed the two-dimensional Fast Fluid Dynamics (2D FFD) into a three-dimensional Fast Fluid Dynamics (3D FFD).The implementation of boundary conditions at outlet was improved with local mass conservation method. A near-wall treatment for Semi-Lagrangian scheme was also proposed. This study validated the 3D FFD with five flows that have features of indoor airflow. The results show that the 3D FFD can successfully capture three dimensionality of the airflow and provide reliable and reasonably accurate simulations for indoor airflows with speed of about 15 times faster than current CFD tools.

Keywords: fast fluid dynamics; building airflow simulations; boundary condition; Semi-Lagrangian

NOMENCLATURE

Roman Symbols

F_i	body force
H	downstream channel height
h	upstream channel height
i, j	index of coordinate
$Mass_{in}$	total mass flow rate into the domain
$Mass_{out}$	total mass flow rate out the domain
N	index of boundary cell
n	previous time step
P	pressure
S	source term
T	temperature
t	time
U_i, U_j	velocity components in x_i and x_j directions, respectively
u	horizontal velocity component or velocity scale
v	vertical velocity component
W	width
w	velocity in the direction normal to the wall
x_i, x_j	spatial coordinates in i and j direction, respectively
x, y, z	spatial coordinates
z_0	coordinate of the wall
z_1	coordinate of the first grid adjacent to the wall
Δt	time step size
Δx, Δy	grid spacing size

Greek Symbols

Γ	transport coefficient

ρ	density
υ	kinetic viscosity
Φ	scalar in transport equation

1. Introduction

Buildings consume approximately 40 percent of primary energy and 70 percent of electricity in the United States. High performance buildings are highly desired since they satisfy thermal comfort and indoor air quality while reducing energy use in buildings. To optimize the design and operation of high performance buildings, it is necessary to have computer tools that can simulate quickly dynamic indoor environmental conditions.

Ideally, the simulations of dynamic indoor environmental conditions in a whole building should be performed in real-time or faster-than-real-time. The real time simulations would allow the building control systems to use the information for optimal control with minimal energy consumption. Although Computational Fluid Dynamics (CFD) has the potential to be used for the simulations, the CFD is too slow with the present computing power in most of the design firms [1, 2]. Therefore, it is necessary to identify a suitable method that can be used to predict the dynamic indoor environmental conditions in a whole building in real time.

One of the possible methods is the multi-zone network models that could significantly decrease the computing time. However, the well mixing assumption of the indoor airflow used in the multi-zone method is not always valid, such as for large indoor spaces or rooms with stratified ventilation systems [2]. In these cases, the multi-zone models may predict inaccurate results [3]. In addition, the Multizone model with the well-mixed assumption cannot provide sufficient information of the micro environment, which is critical for thermal comfort and air quality.

Zonal models [4] , dividing a room into a limited number of subzones, can provide improvement over the well mixed assumption used by multi-zone model and also achieve fast simulation. However, because the zonal models do not solve the conservation equations for momentum, the accuracy suffers for the flows with strong momentum [2].

In addition, the coarse-grid CFD is gaining attention from researchers and is promising to replace the zonal models [2]. With very coarse grids, the computing time of CFD simulations could be reduced significantly, but the grid independency would be sacrificed and unknown errors would be induced by the low grid resolution [5].

Another possible method for real-time indoor environment simulations is Fast Fluid Dynamics (FFD). The method, originally used for computer games, could be used for the simulations of indoor environmental conditions. Zuo et al. [6,7,8] developed a two-dimensional Fast Fluid Dynamics (2D FFD) for airflow simulations in buildings. Their results showed that the computing speed was 50 times faster than the two-dimensional CFD and real-time simulation of indoor airflow seems possible. Although the results were not as accurate as those of CFD, they were much better than those produced by the multi-zone model.

However, airflows in buildings are complex and always three dimensional [9]. In order to capture the characteristics of the three-dimensional airflows, it is necessary to extend the 2D FFD code into a three dimensional one. To demonstrate the capabilities and accuracy of the 3D FFD code, it is essential to apply it to a few cases of indoor airflows with high quality reference data. This forms the basis of current investigation reported in this paper.

2. Research Method

The following section discussed the fundamentals of FFD and the implementation of the 3D code that have new algorithms to handle different boundary conditions normally encountered in indoor environment.

2.1 Governing equations for fast fluid dynamics

The FFD was introduced by Stam [10] for computer games, aimed to simulate incompressible fluid flows with a simple and stable approach. In fact, the FFD is a form of projection method introduced by Chorin [11] in early 1960s to solve the incompressible Navier-Stokes (NS) equations (1) and continuity equation (2) given below:

$$\frac{\partial U_i}{\partial t}+U_j\frac{\partial U_i}{\partial x_j}=-\frac{1}{\rho}\frac{\partial p}{\partial x_i}+\upsilon\frac{\partial^2 U_i}{\partial x_j\partial x_j}+\frac{1}{\rho}F_i\,, \tag{1}$$

$$\frac{\partial U_i}{\partial x_i}=0\,, \tag{2}$$

where U_i and U_j are velocity, p pressure, ρ density, F_i body forces, and x_i and x_j spacial coordinates, respectively. Projection method is an efficient approach to solve incompressible flows[12,13]. In the projection method, instead of solving a coupled system of Navier-Stokes equations for velocity and pressure, typically a sequential two-stage method is applied. At first, an intermediate velocity field is computed from the momentum equations ignoring the incompressibility constrain, and then pressure projection is used to project the intermediate velocity field into a space of divergence free vector field to obtain pressure and updated velocity. However in the FFD, a three-step method is used by solving the following three equations in each step:

$$\frac{U_i^*-U_i^n}{\Delta t}=-U_j^n\frac{\partial U_i^n}{\partial x_j}\,, \tag{3}$$

$$\frac{U_i^{**}-U_i^*}{\Delta t}=\upsilon\frac{\partial^2 U_i^{**}}{\partial x_j\partial x_j}+\frac{1}{\rho}F_i\,, \tag{4}$$

$$\frac{U_i^{n+1}-U_i^{**}}{\Delta t}=-\frac{1}{\rho}\frac{\partial p}{\partial x_i}, \tag{5}$$

where U^n and U^{n+1} represents velocity at previous time step and current time step, respectively, and U^* and U^{**} are intermediate velocities. At the first step, the FFD uses the first-order Semi-Lagrangian scheme to solve equation (3) for convection, and the velocity at previous time step is updated with U^*. At the second step, the fully implicit scheme is used to solve equation (4) for the diffusion with the source term, and the intermediate velocity is further updated with U^{**}. At the third step, the pressure projection is conducted. From equations (2) and (5), it is easy to derive the following Poisson equation:

$$\frac{\partial^2 p}{\partial x_j\partial x_j}=\frac{\rho}{\Delta t}\frac{\partial U_i^{**}}{\partial x_i}. \tag{6}$$

The pressure obtained from solving the Poisson equation is then used to update velocity field with equation (5). After obtaining the velocity field, transport equations for other scalars can be further solved similarly:

$$\frac{\partial \Phi}{\partial t}+U_j\frac{\partial \Phi}{\partial x_j}=\Gamma\frac{\partial^2 \Phi}{\partial x_j\partial x_j}+S\,, \tag{7}$$

where Φ is the scalar to be solved, Γ the transport coefficient, and S the source term, respectively.

The current study did not include the turbulence model in the FFD. Instead, the FFD uses numerical viscosity [14] as a substitute of turbulent viscosity. The numerical viscosity will decrease when the grid is refined.

2.2 Implementation of the three dimensional code

The extension from the 2D FFD to the 3D FFD was straightforward as all the governing equations were identical. The 3D FFD used a finite-volume discretization scheme, which essentially satisfied conservation laws. The 3D FFD also applied staggered grid [15] to store velocity on the grid faces and other variables at the grid center.

In addition, the 3D FFD code introduced different markers for identifying boundary and interior cells to handle complex geometries. As illustrated in Figure 1, cells in the interior of the fluid region were assigned value 1 to a marker, and cells at the boundary and inside the obstacle with grey colour were marked as 0. With this approach, the code could automatically identify boundary cells and interior cells during computation, which would deal with obstacles flexibly in the computational domain.

2.3. Implementation of boundary conditions

Boundary conditions are crucial in solving incompressible Navier-Stokes equations [16]. In FFD, paired boundary conditions for both velocity and pressure are required to solve implicit diffusion equations and Poisson equation [17],[18]. Different velocity and pressure boundary conditions would be assigned for different type of boundaries. For airflow simulations in buildings, the computation domains are typically bounded by solid walls and openings, such as inlets and outlets. For the solid walls, non-slip boundary is usually applied. For inlets, constant velocity is enforced. Both of these two boundary conditions can be categorized as Dirichlet boundary condition. The 3D FFD used the physical velocity boundary condition as boundary condition for intermediate velocity as the following:

$$U_i^{**}|_b = U_i^{n+1}|_b = U_{bi} . \tag{8}$$

The Neumann boundary condition for pressure was derived from equations (5) and (8):

$$\frac{\partial p}{\partial n}|_b = 0 . \tag{9}$$

At outlets, usually outflow boundary condition is applied. However, the implementation of outflow boundary condition in the FFD can be done in multiple ways. The most common implementation of the velocity at outflow boundary is a simple Neumann boundary condition with its gradient set to be zero. This approach is based on the assumption that the outlet is located at fully developed regions. However, this is usually not the case in building airflow simulations because the locations of outlet are often at circulation regions. Therefore, this investigation applied the local mass conservation for the outflow boundary for velocity as suggested by Li et al. [19].

Figure 2 illustrates the implementation of local mass conservation method. The normal derivative of tangential velocity at the outlet was set to zero. The velocity component normal to the outlet was firstly derived by applying mass conservation at the cells adjacent to the outlet:

$$u_{N,j} = u_{N-1,j} + \frac{\Delta x}{\Delta y}(v_{N,j-1} - v_{N,j}). \tag{10}$$

However the boundary velocity derived from equation (10) would not ensure overall mass conservation. This study further corrected the boundary normal velocity through mass correction equation:

$$u_{N,j} = u_{N,j} \times \frac{Mass_{in}}{Mass_{out}}, \tag{11}$$

where $Mass_{in}$ is the total mass-flow rate at all the inlets and $Mass_{out}$ the total mass-flow rate at all the outlets, respectively. Since the mass conservation constraint had already been applied at the outlet boundary cells, it was not necessary to update the normal velocity at the outlet boundary through pressure projection. Similarly, Neumann boundary conditions could be derived for pressure at outflow boundaries as shown by equation (9).

2.4 Treatment of Semi-Lagrangian scheme at near-wall regions

FFD used a Semi-Lagrangian scheme [20] to solve the advection equations. Figure 3 demonstrated the principle of Semi-Lagrangian scheme. The backward trajectory approach was designed to determine the departure locations of particles that arrive at grid points at the new time step. The velocity and other scalars at the departure point could be interpolated from those known at surrounding grid cells.

The one-time-step Semi-Lagrangian scheme can provide only the first-order time accuracy. The truncation error might lead to a high probability that the tracing back from the arrival location near a solid wall could be located outside of the flow domain, as depicted in Figure 4(a). The FFD would then relocate any departure points outside the boundary to the nearest wall boundary, but this might result in too low velocity in the domain where many departure points were located on the solid wall boundary [21].

In order to avoid having departure points located outside the boundary, the 3D FFD employed a special treatment for the Semi-Lagrangian scheme at the near wall region. The treatment assumed that the velocity component normal to the wall varied linearly between the wall boundary and the first grid adjacent to the wall. If the backward trajectory crossed the first grid close to the wall boundary, the tracing back velocity in the normal wall direction would

linearly decrease to zero at wall surface. Thus the departure point would not locate outside the domain.

As illustrated in Figure 4(b), the trace-back process in the normal wall direction (z direction) was first performed with the velocity, w_a, at arrival point. Once the trace-back trajectory crossed the first grid adjacent to the wall, the equation (12) was used to calculate the new trace-back velocity:

$$w=\frac{z-z_0}{z_1-z_0}w_1, \tag{12}$$

where z is coordinate in normal wall direction, z_0 the coordinate of wall boundary in normal wall direction, z_1 the coordinate of first grid adjacent to wall in normal wall direction and w_1 the velocity at the point where the trajectory crossed the first grid adjacent to the wall, respectively. The equation (12) was then integrated over the remained trace-back time to derive the coordinate of departure point:

$$z_d=z_0+(z_1-z_0)\exp\left[-\frac{v_1}{z_1-z_0}(\Delta t-\frac{z_a-z_1}{w_a})\right], \tag{13}$$

where z_d is the coordinate of departure point in normal wall direction, z_a the coordinate of arrival point in normal wall direction and Δt the time step size, respectively.

3. Results

With the numerical method outlined in the previous section, this investigation evaluated the performance of the 3D FFD for five cases with reference data from the literature. The cases are: (1) a simple lid driven cavity flow that shows a typical room airflow pattern with mixing ventilation by a wall jet, (2) a backward facing step flow that looks like a jet coming from a duct to a room, (3) a forced convection flow in an empty room that is more realistic in buildings, (4) a forced convection flow in a room with a box that represents a piece of furniture, and (5) a mixed convection flow in a room with a heated box that represents occupant or heated equipment. The test cases with laminar flows can help to test the performance of the numerical scheme used in FFD. Because no turbulence models were integrated in 3D FFD in this study, we did not intentionally test it with fully developed turbulent flows.

3.1 Case 1: Airflow in a lid driven cavity

The lid-driven cavity flow is one of the most important benchmark cases for numerical solvers of Navier-Stokes equation. The flow has a simple computational domain of square geometry and single driving force by means of tangential movement of the lid with constant velocity. Thus only Dirichlet boundary conditions for velocity were applied in the 3D FFD. Ku et al. [22] studied the three dimensional lid driven cavity flows with Chebyshev pseudo-spectral technique and found that the flow was more affected by three dimensional boundaries with increasing Reynolds number from 100 to 1000. As shown in Figure 5, this investigation used the similar cubic cavity as Hwar et al. [22] for the test case. The size of the cavity was 1 m × 1 m × 1 m and the Reynolds number based on the cavity dimension was 1000. In order to evaluate the capability of the 3D FFD in predicting the three dimensional flows, both the 3D FFD and the 2D FFD were used to simulate the airflow.

Figure 6 shows the simulated velocity profiles using different grid resolutions with the 3D FFD for Case 1. The result was not improved much when increasing grid resolution from 60×60×60 to 80×80×80. So the 60×60×60 were considered to be sufficient fine for this case. Using finer grid can improve the accuracy, but slow down the speed. Since the FFD is designed for fast flow simulation and coarse grid is always preferred in its application, the rest of the case studies use coarse grids. The results can be further improved by using finer grids.

Figure 7 compares velocity profiles simulated by the 2D FFD with 60×60 grids and the 3D FFD with 60×60×60 grids at the vertical and horizontal centerlines of the cavity. The high accuracy simulation data from Ku et al. [22] was used as a reference. Figure 7(a) shows that the 2D FFD obtained a higher peak velocity at Y/L=0.2 and higher velocity at Y/L=0.8 than the 3D FFD and reference data, because the 2D FFD could not predict viscous effect from the side walls. Due to the same reason, the 2D FFD predicted an average higher velocity value at the center region of the cavity than the 3D FFD and reference data in Figure 7(b). Because of the existence of numerical diffusivity in the FFD, there was some discrepancy between the results

of the 3D FFD and reference data. For instance, in Figure 7(a), the velocity at Y/L=0.4 was under-predicted by the 3D FFD, and in Figure 7(b), the peak velocity near both right and left wall were also under-estimated by the 3D FFD. Overall, the result from the 3D FFD was more accurate than that of the 2D FFD, because it was able to predict the three dimensionality of airflow cased by side wall effects.

3.2 Case 2: Airflow through backward facing step

The backward facing step flow comprises separation, recirculation, and subsequently reattachment, which are fundamental features of complex airflows in buildings. It also has both openings and walls. Thus, this flow would be a good test case for the 3D FFD before it was tested for real flows in buildings. Armaly et al. [23] conducted experimental investigation of the backward-facing step flow and obtained high quality data. This study applied the same settings as in their experiment for the test case. As depicted in Figure 8, the channel height in the upstream of the step, h, was 5.2 mm and the downstream channel height, H, was 10.1 mm, giving the expansion ratio of 1.94. The width of the channel, W, was 180 mm, giving the aspect ratio of 18:1. At the inlet, fully developed velocity profile was applied for velocity boundary condition and outflow boundary condition was used at the downstream outlet. Similar to the previous test case, both the 2D FFD and 3D FFD were applied to simulate the flow features in the backward facing step. The grids of 40×40×20 and 40×20 were used for the 3D FFD and 2D FFD, respectively.

Figure 9 shows the dependence of the normalized primary reattachment length on Reynolds number. The results from the 2D FFD and 3D FFD results are compared with experimental data. At low Reynolds numbers (Re = 100 and 300), both the 3D FFD and 2D FFD results had excellent agreement with the experimental data. However, when the Reynolds number became higher than 400, the 3D FFD results still agreed with the experimental data, but the 2D FFD results diverged from the data. As pointed out by Armaly et al. [23], at higher Reynolds number, the sidewall of the channel would induce three dimensionality of the flow, affecting the flow structure at the channel mid-plane. Obviously, the 2D FFD was incapable to capture the three-dimensional features.

3.3 Case 3: Forced convection in the empty room.

In order to evaluate the 3D FFD for more realistic cases, this study tested 3D FFD with cases from Wang et al. [24]. They investigated experimentally the airflows with adding features in a room: (A) isothermal forced convection in the empty room; (B) isothermal forced convection in the room with a box; (C) mixed convection in the room with the heated box.

Figure 10(a) shows the case of forced convection in the empty room. An isothermal jet was generated at the inlet at upper left corner and developed along the ceiling, reaching far right. The air then turned downwards because of the existence of right wall and further formed a circulation in the room. This was a basic airflow pattern in a mechanically ventilated room. The room size was 2.44 m × 2.44 m × 2.44 m and the inlet and outlet heights were 0.03 m and 0.08 m, respectively. The inlet air velocity was 0.455 m/s with the corresponding Reynolds number around 2,000. The local mass conservation method was applied at the outlet. In order to compare the performance of the 3D FFD with the CFD tools, a laminar CFD simulation using ANSYS Fluent 12.1 was also performed for this test case. The grids of 20×20×20 were used for both the 3D FFD and the laminar CFD calculations.

Figure 10 (b) shows 10 measurement positions in the experiments. The velocities at positions 1, 3, 5 and 6 were selected since they were in the jet upstream, jet downstream, room center and a position close to the side wall, respectively. Figure 11 shows the velocity profiles at the four measurement positions predicted by the 3D FFD and the laminar CFD. Figure 11 showed that 3D FFD predicted similar airflow as the laminar CFD in this case. Both of them could predict general velocity variation in the vertical direction and capture the high speed of the jet from inlet. Their results matched with experimental data quite well at position 3, located in the center of the room. At the near-wall region with relatively high gradient (position 5), both the 3D FFD and the laminar CFD could not obtain a good agreement with the experiment data. Similarly, Wang et al. [24] also found that the CFD simulation with turbulence models did

not do a good job at position 5. This was because the flow structure was much complex near the right wall, where separation occurred.

3.4 Case 4: Forced convection in the room with box.

This test case was Case B from Wang et al. [24]. As illustrated in Figure 12, a box was added in the center of the room, and it would cause airflow separation that was similar as the airflow in a room blocked by obstacles like furniture and occupants. So in this case, the 3D FFD could be further tested with increasing airflow features and more complex geometry of computational domain. The room size was identical with the one in previous case, and the dimension of box was 1.22 m × 1.22 m × 1.22 m. The inlet and outlet boundary conditions were also the same with the settings in the previous case. Similarly, this test case was also simulated with laminar CFD using ANSYS FLUENT 12.1[25], and the grids of 20×20×20 were used for both the 3D FFD and the laminar CFD simulations.

Figure 13 reported the velocity profiles at the four locations predicted by 3D FFD and laminar CFD simulations. The results were compared with the experiment data. The 3D FFD under-predicted the air velocity at position 1 and 5, because the airflow was complex at position 5, where the airflow was blocked by the box and formed a secondary circulation between the box and right wall. Also this under-prediction might imply that the current scheme is so diffusive that the air velocity affected a lot by the solid wall. At other two positions the agreement was acceptable with only some discrepancies at near-floor-region. The 3D FFD computed the velocities slightly better than the laminar CFD simulation for this case.

3.5 Case 5: Mixed convection in the room with box.

In Case C from Wang et al. [24], a heat source of 700W was added in the box in Case B. The heated box would generate thermal plumes as often found from different heating sources in buildings, such as occupants and electric appliances, etc. The supply air temperature was controlled at 22.2 ^{o}C; the temperature of box surface, ceiling, surrounding walls and floor were 36.7, 25.8, 27.4 and 26.9 ^{o}C, respectively. All other boundary conditions were the same as Case B. The grids of 20 × 20 × 20 were used for both the 3D FFD and the laminar CFD simulation in this case.

In Figure 14, the vertical velocity profiles predicted by the 3D FFD agree with the experimental data except at position 5. Similar to Case B, the failure of 3D FFD at position 5 might caused by its incapability of modelling complex flow structure. Compared with the laminar CFD simulations, the 3D FFD obtained more accurate results.

This case was non-isothermal so the temperature profiles predicted was compared with the experimental data in Figure 15 at the four positions. The temperature was normalized and defined as $T^*= (T-T_{min})/ (T_{max}-T_{min})$, where T_{min} = 22.2^{o}C and T_{max} = 36.7 ^{o}C were the minimum and maximum temperature found in this case, respectively. Because of lack of turbulence model, the laminar CFD could not predict the surface heat transfer coefficient correctly and thus under predicted the temperature magnitude. It is also difficult for the 3D FFD to correctly predict surface heat transfer for the same reason. This study thus applied a treatment in this case that the thermal diffusivity between the first grid and the wall was adjusted to obtain a good agreement between the predicted temperature magnitude and the experimental data.

4. Discussions

The above tests showed that the 3D FFD was reasonably accurate and reliable for simulating airflows in buildings. Although the main objective of the 3D FFD was not to pursue accuracy, the comparison with results of laminar CFD showed that the overall performance of 3D FFD in simulating real flow in the last three cases was better. This seemed a little strange because no turbulence models were used in the current 3D FFD. The possible explanation was that the numerical viscosity generated by the FFD scheme acted as adding turbulent viscosity into the flows and thus predicted more realistic flows. However, not in all cases, numerical viscosity would positively affect airflow simulations. In the lid driven cavity, the FFD scheme was so diffusive that under-predicted the peak velocities.

The major advantage of the FFD compared to the CFD is its speed. This study also conducted a comparison of simulation speed between the 3D FFD and the laminar CFD. Table 1 reported the computing time of the test cases. All three cases used same time step size of 0.1

seconds and grid size of 20×20×20, and both the 3D FFD and the laminar CFD simulations were performed on a personal computer with a single Intel CPU at 3.00 GHz. Comparing the elapsed flow time and the elapsed CPU time, the 3D FFD could realize faster-than-real time simulations for the grid size and time steps. On the other hand, the laminar CFD was 14-18 times slower than the 3D FFD.

5. Conclusion

It is essential to extend the capability of FFD in modelling three dimensional flows before its application in indoor airflow simulations in real buildings. In this paper, the 3D FFD was developed from a previously developed two dimensional model.

The 3D FFD adopted the finite volume discretization scheme on the staggered grid, and improved the data structure to handle computational domain with more complex geometry. Local mass conservation method was applied to improve the implementation of boundary condition at outlet. This study also proposed approximation on the near wall treatment for Semi-Lagrangian scheme to avoid having departure points located outside the boundary.

Through the tests of lid-driven cavity and backward facing step, the 3D FFD successfully predicted the side-wall viscous effect and proved its capability of capturing three dimensionality of air flow. The 3D FFD could achieve higher accuracy than the 2D FFD on modelling the three dimensional flows.

The 3D FFD was also tested for more realistic flows in buildings, which covered flow features including jet flow, flow separation and thermal plumes, etc. The results showed that the 3D FFD could provide reliable and acceptably accurate simulations in these cases, and is potential for simulating airflows in buildings. The computing speed was about 15 times faster than the laminar CFD.

References

[1] Z. Zhai and Q. Chen, Sensitivity analysis and application guides for integrated building energy and CFD simulation, *Energy and Buildings*, vol. 38, pp. 1060-1068, 2006.

[2] Q. Chen, Ventilation performance prediction for buildings: A method overview and recent applications, *Building and Environment*, vol. 44, pp. 848-858, 2009.

[3] L. Wang and Q. Chen, Evaluation of some assumptions used in multizone airflow network models, *Building and Environment*, vol. 43, pp. 1671-1677, 2008.

[4] A. C. Megri and F. Haghighat, Zonal modeling for simulating indoor environment of buildings: review, recent developments, and applications, *HVAC&R Research*, vol. 13, pp. 887–905, 2007.

[5] H. Wang and Z. Zhai, Analyzing grid independency and numerical viscosity of computational fluid dynamics for indoor environment applications, *Building and Environment,* vol. 52, pp. 107–118, 2012.

[6] W. Zuo and Q. Chen, Real‐time or faster‐than‐real‐time simulation of airflow in buildings, *Indoor Air*, vol. 19, pp. 33-44, 2009.

[7] W. Zuo and Q. Chen, Fast and informative flow simulations in a building by using fast fluid dynamics model on graphics processing unit, *Building and Environment*, vol. 45, pp. 747-757, 2010.

[8] W. Zuo, J. Hu, and Q. Chen, Improvements in FFD Modeling by Using Different Numerical Schemes, *Numerical Heat Transfer, Part B: Fundamentals*, vol. 58, pp. 1–16, Aug. 2010.

[9] Z. Zhai, W. Zhang, Z. Zhang, and Q. Chen, Evaluation of Various Turbulence Models in Predicting Airflow and Turbulence in Enclosed Environments by CFD: Part 1--Summary of Prevalent Turbulence Models, *HVAC&R Research*, vol. 13, pp. 853-870, 2007.

[10] J. Stam, Stable fluids, The 26th annual conference on Computer graphics and interactive techniques, Los Angeles, 1999, pp. 121-128.

[11] C. Alexandre, A numerical method for solving incompressible viscous flow problems, *Journal of Computational Physics*, vol. 2, pp. 12-26, 1967.

[12] J. L. Guermond, P. Minev, and J. Shen, An overview of projection methods for incompressible flows, *Computer Methods in Applied Mechanics and Engineering*, vol. 195, pp. 6011–6045, 2006.

[13] N. Sekarapandian, Y. V. S. S. Sanyasiraju, and S. Vengadesan, A Novel Semi-Explicit Spatially Fourth Order Accurate Projection Method for Unsteady Incompressible Viscous Flows, *Numerical Heat Transfer, Part A: Applications*, vol. 56, pp. 665–684, 2009.
[14] W. Zuo and Q. Chen, Simulations of Air Distributions in Buildings by FFD on GPU, *HVAC&R Research*, vol. 16, no. 6, pp. 785–798, 2010.
[15] F. H. Harlow and J. E. Welch, Numerical Calculation of Time-Dependent Viscous Incompressible Flow of Fluid with Free Surface, *Physics of Fluids*, vol. 8, p. 2182, 1965.
[16] D. Rempfer, On Boundary Conditions for Incompressible Navier-Stokes Problems, *Applied Mechanics Reviews*, vol. 59, pp. 107-125, 2006.
[17] Y. B. Kim and M. J. Lee, Boundary-condition pairs for fractional step methods and compatibility with the pressure Poisson equation, *Computational Fluid Dynamics Journal*, vol. 11, pp. 323-334, 2002.
[18] R. Temam, Remark on the pressure boundary condition for the projection method, *Theoretical and Computational Fluid Dynamics*, vol. 3, pp. 181-184, 1991.
[19] P. W. Li and W. Q. Tao, Effects of outflow boundary condition on convective heat transfer with strong recirculating flow, *Heat and Mass Transfer*, vol. 29, pp. 463-470, 1994.
[20] A. Staniforth and J. Côté, Semi-Lagrangian Integration Schemes for Atmospheric Models—A Review, *Monthly Weather Review*, vol. 119, pp. 2206-2223, 1991.
[21] N. Wood, A. Staniforth, and A. White, Determining near‐boundary departure points in semi‐Lagrangian models, *Quarterly Journal of the Royal Meteorological Society*, vol. 135, pp. 1890-1896, 2009.
[22] H. C. Ku, R. S. Hirsh, and T. D. Taylor, A pseudospectral method for solution of the three-dimensional incompressible Navier-Stokes equations, *Journal of Computational Physics*, vol. 70, pp. 439-462, 1987.
[23] B. F. Armaly, F. Durst, J. C. F. Pereira, and B. Schönung, Experimental and Theoretical Investigation of Backward-Facing Step Flow, *Journal of Fluid Mechanics*, vol. 127, pp. 473-496, 1983.
[24] M. Wang and Q. Chen, Assessment of various turbulence models for transitional flows in an enclosed environment, *HVAC&R Research, vol*. 15, pp. 1099-1119, 2009.
[25] ANSYS, ANSYS FLUENT 12.1 Documentation, ANSYS Inc., PA.

Table 1 Comparison of computing time by 3D FFD and laminar CFD

Test cases	Elapsed flow time (s)	Elapsed CPU time (s)	
		3D FFD	CFD
Forced convection in empty room	100	29	474
Forced convection in room with box	100	31	439
Mixed convection in room with box	100	31	555

Caption of figures

Figure 1 The boundary cells and interior cells in the computational domain
Figure 2 Boundary control volume for local mass conservation method
Figure 3 Schematic of Semi-Lagrangian scheme
Figure 4 Schematic of near wall treatment for the Semi-Lagrangian scheme
Figure 5 Schematic of the flow in cubic lid-driven cavity
Figure 6 Grid independence study for the lid-driven cavity case
Figure 7 Comparison of velocity variation in the lid-driven cavity predicted by 3D FFD and 2D FFD with data from Ku et al. [22]: (a) vertical centerline and (b) horizontal centreline
Figure 8 Schematic of the backward fasting step
Figure 9 Comparison of primary reattachment length predicted by 3D FFD and 2D FFD with the data from Armaly et al. [23]
Figure 10 Schematic of the test chamber for the forced convection and the measurement positions
Figure 11 Comparison of velocity profiles in case A predicted by 3D FFD and CFD with the experiment data from Wang et al. [24] at positions (a) 1, (b) 3, (c) 5, and (d) 6, respectively
Figure 12 Schematic of the test room with a box
Figure 13 Comparison of velocity profiles in case B predicted by 3D FFD and CFD with the experiment data from Wang et al. [24] at positions (a) 1, (b) 3, (c) 5 and (d) 6, respectively
Figure 14 Comparison of velocity profiles in case C predicted by 3D FFD and CFD with the experiment data from Wang et al. [24] at positions (a) 1, (b) 3, (c) 5 and (d) 6, respectively
Figure 15 Comparison of temperature profiles in case C predicted by 3D FFD and CFD with the experiment data from Wang et al. [24] at positions (a) 1, (b) 3, (c) 5 and (d) 6, respectively

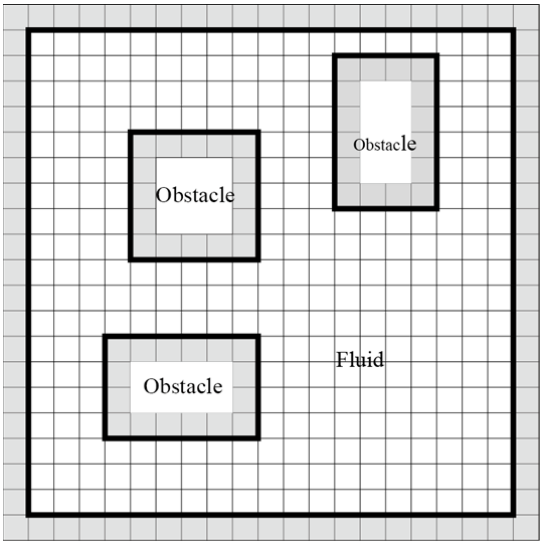

Figure 1

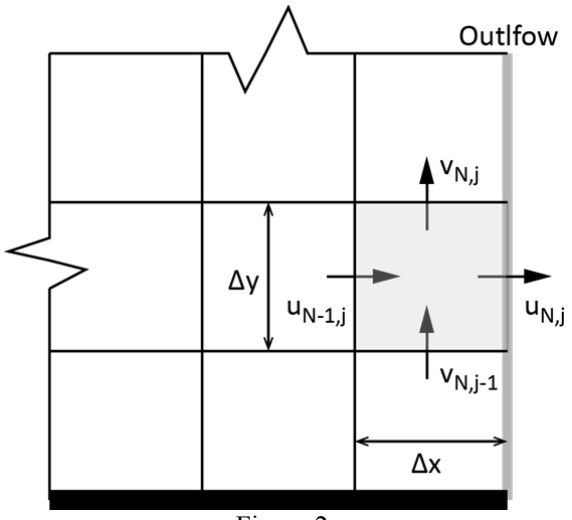

Figure 2

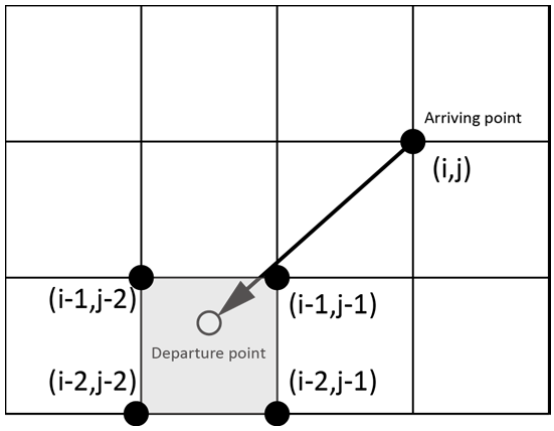

Figure 3

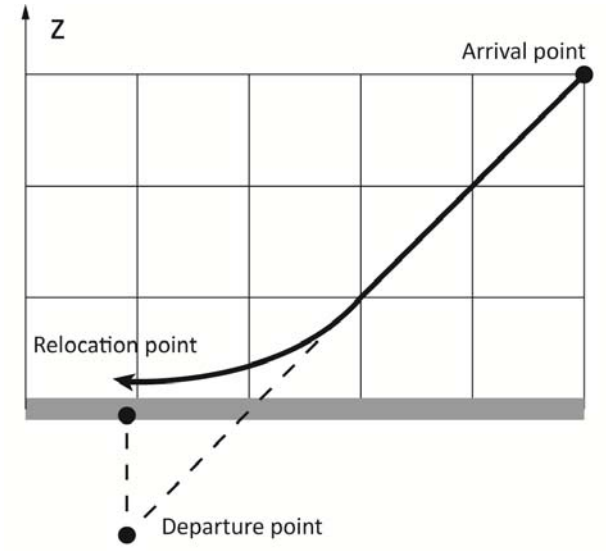
Z
Arrival point
Relocation point
Departure point

(a)

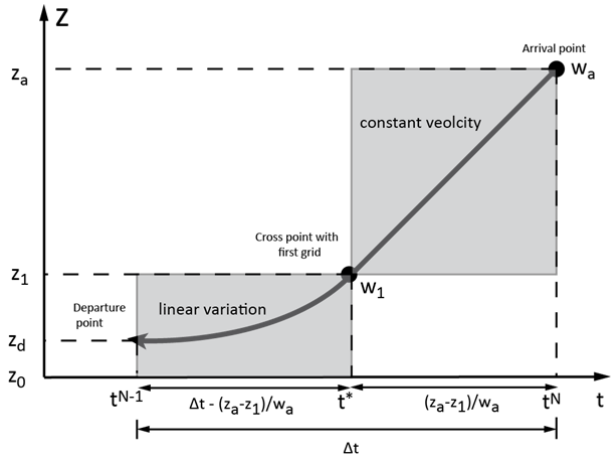
Z
Arrival point
z_a
w_a
constant veolcity
Cross point with first grid
z_1
w_1
Departure point
linear variation
z_d
z_0
t^{N-1}
$\Delta t - (z_a - z_1)/w_a$
t^*
$(z_a - z_1)/w_a$
t^N
t
Δt

(b)

Figure 4

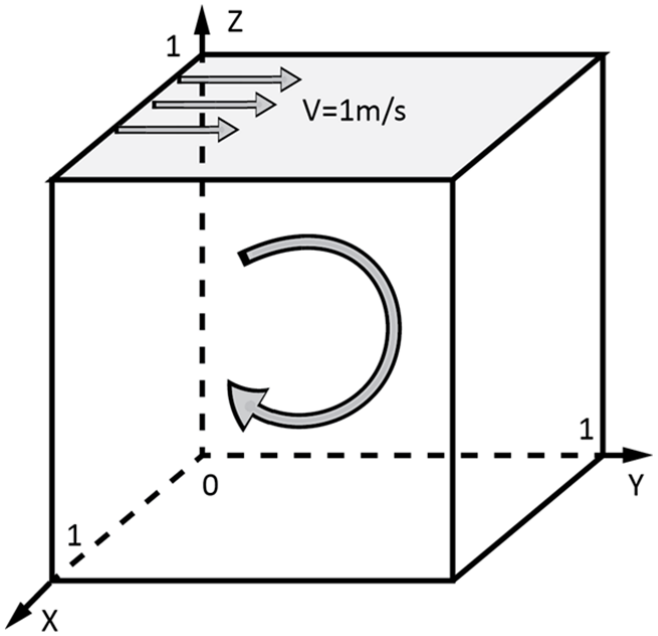

Figure 5

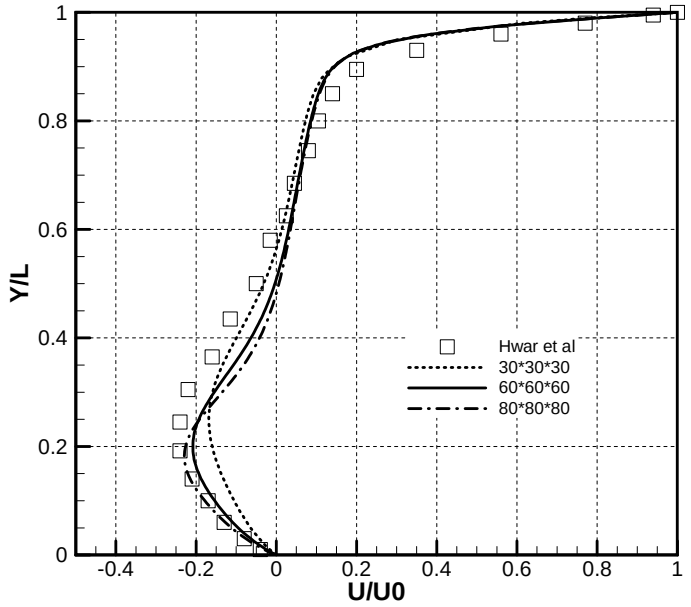
Y/L
U/U0
Hwar et al
30*30*30
60*60*60
80*80*80
0
0.2
0.4
0.6
0.8
1
-0.4
-0.2
0
0.2
0.4
0.6
0.8
1

Figure 6

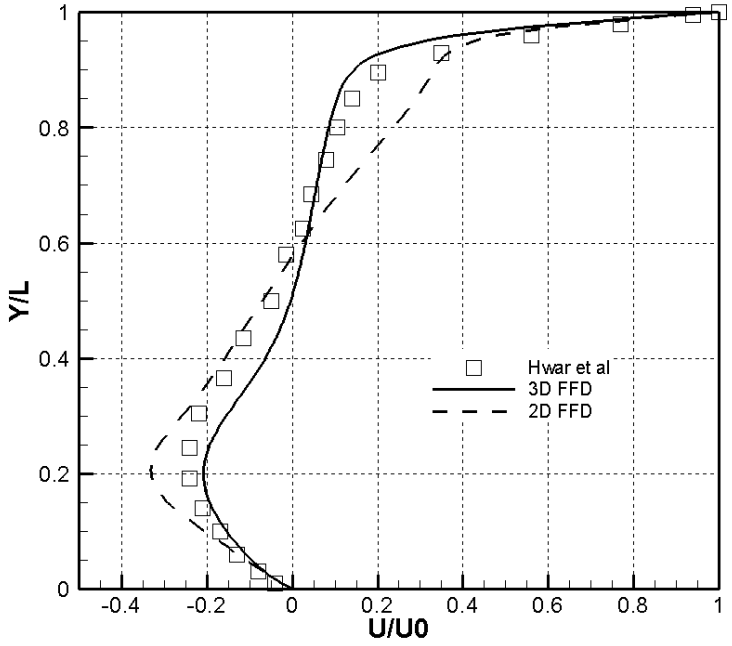

(a)

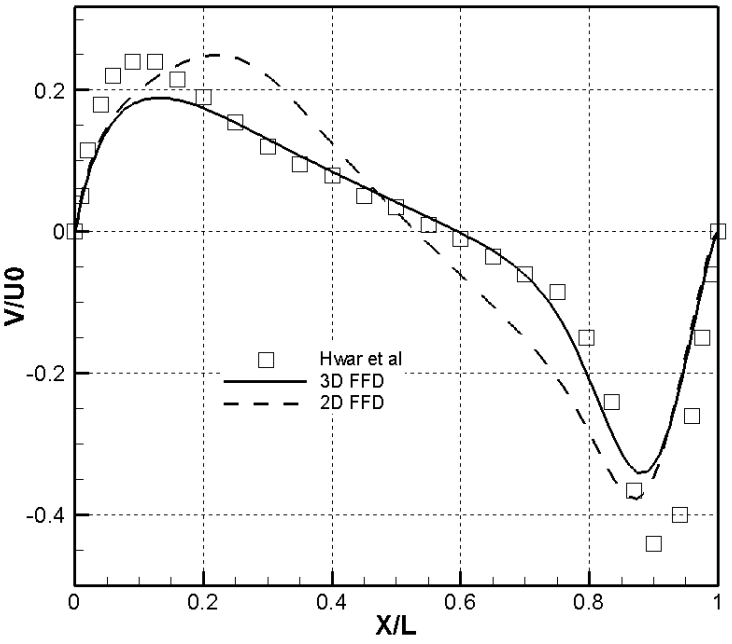

(b)

Figure 7

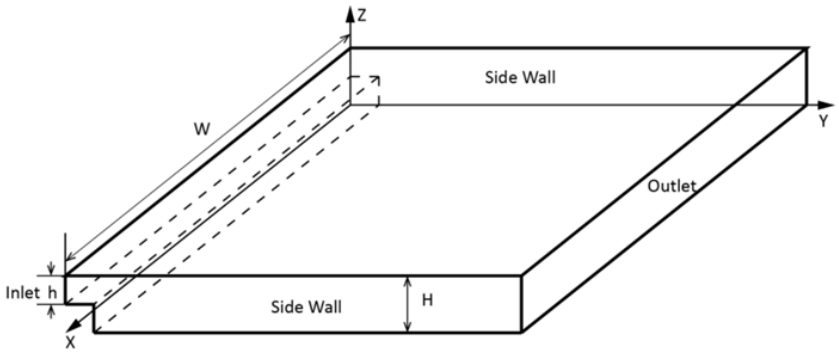

Figure 8

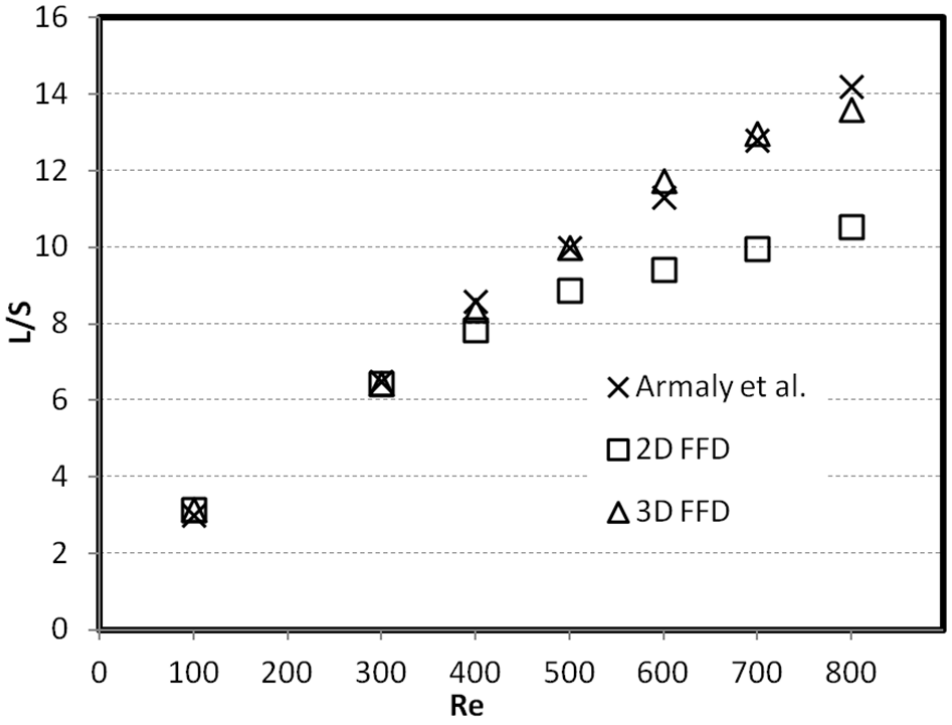
16
14
12
10
8
6
4
2
0
L/S
0
100
200
300
400
500
600
700
800
Re
Armaly et al.
2D FFD
3D FFD
Figure 9

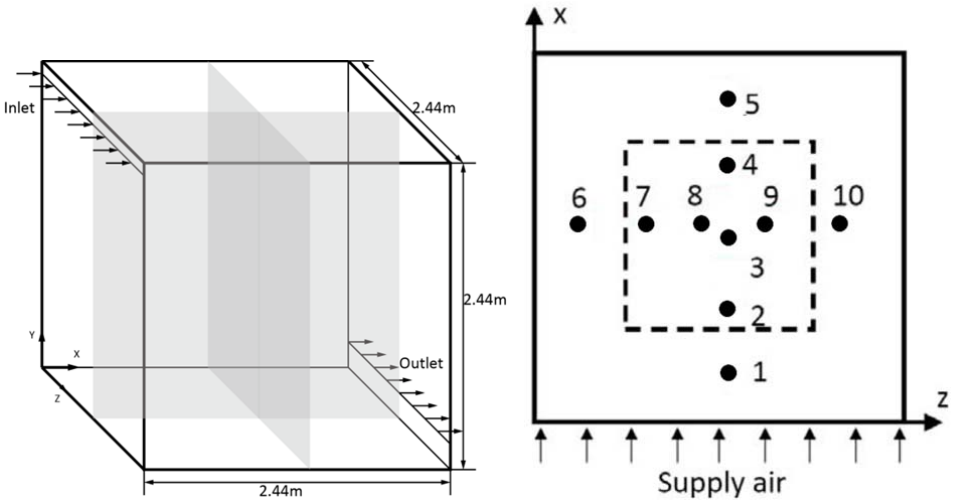

(a) (b)

Figure 10

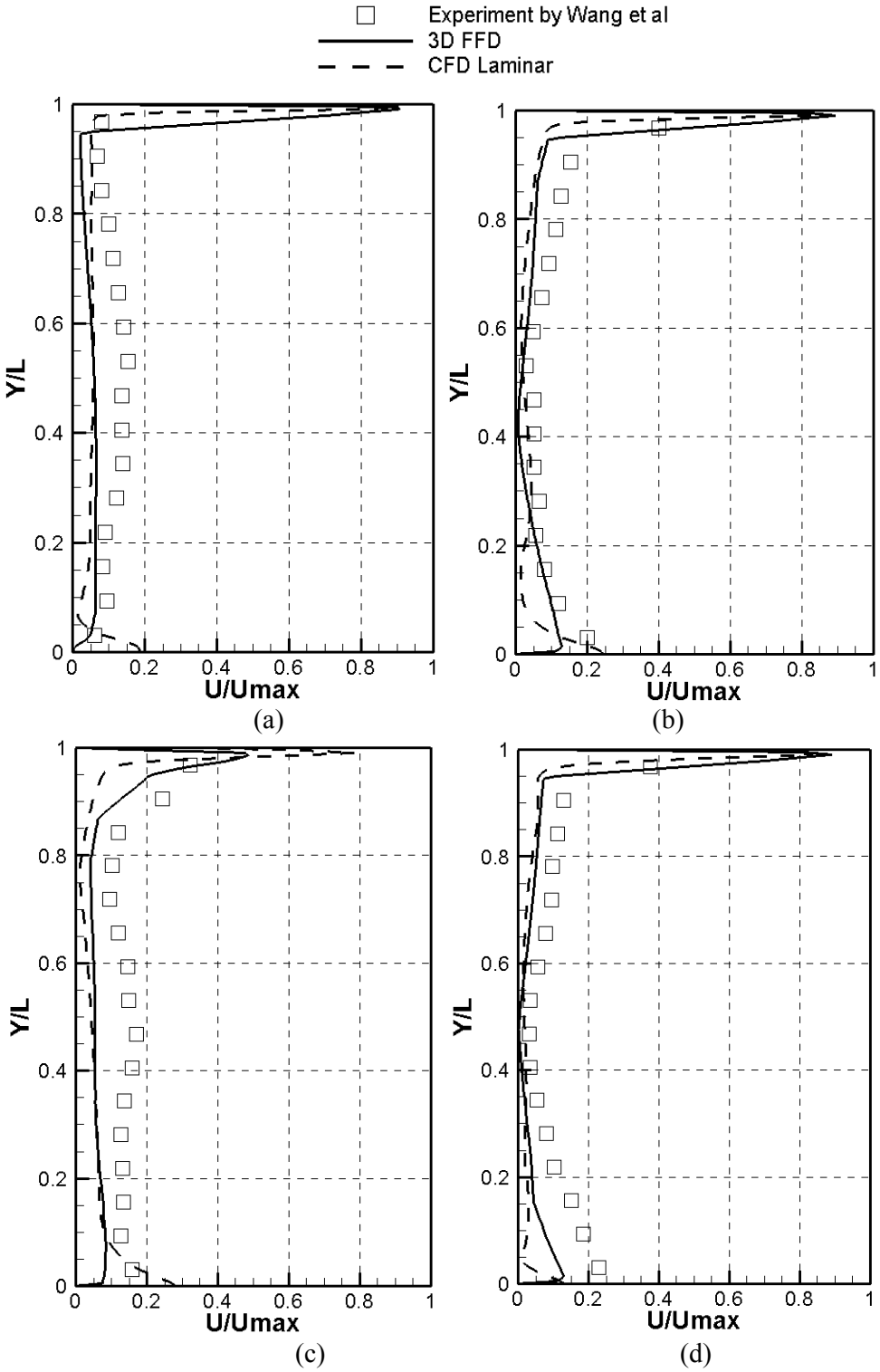

Figure 11

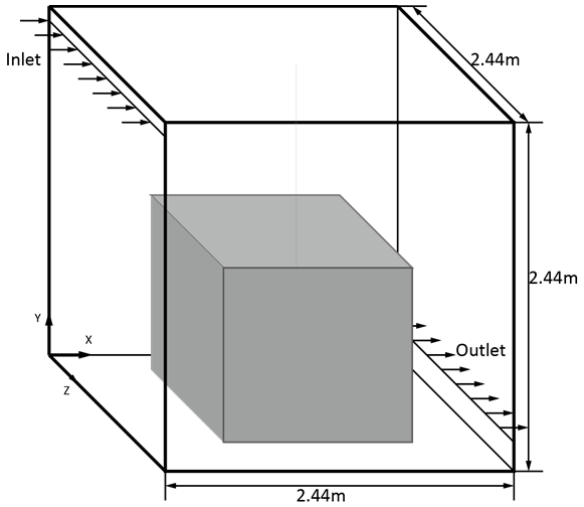

Figure 12

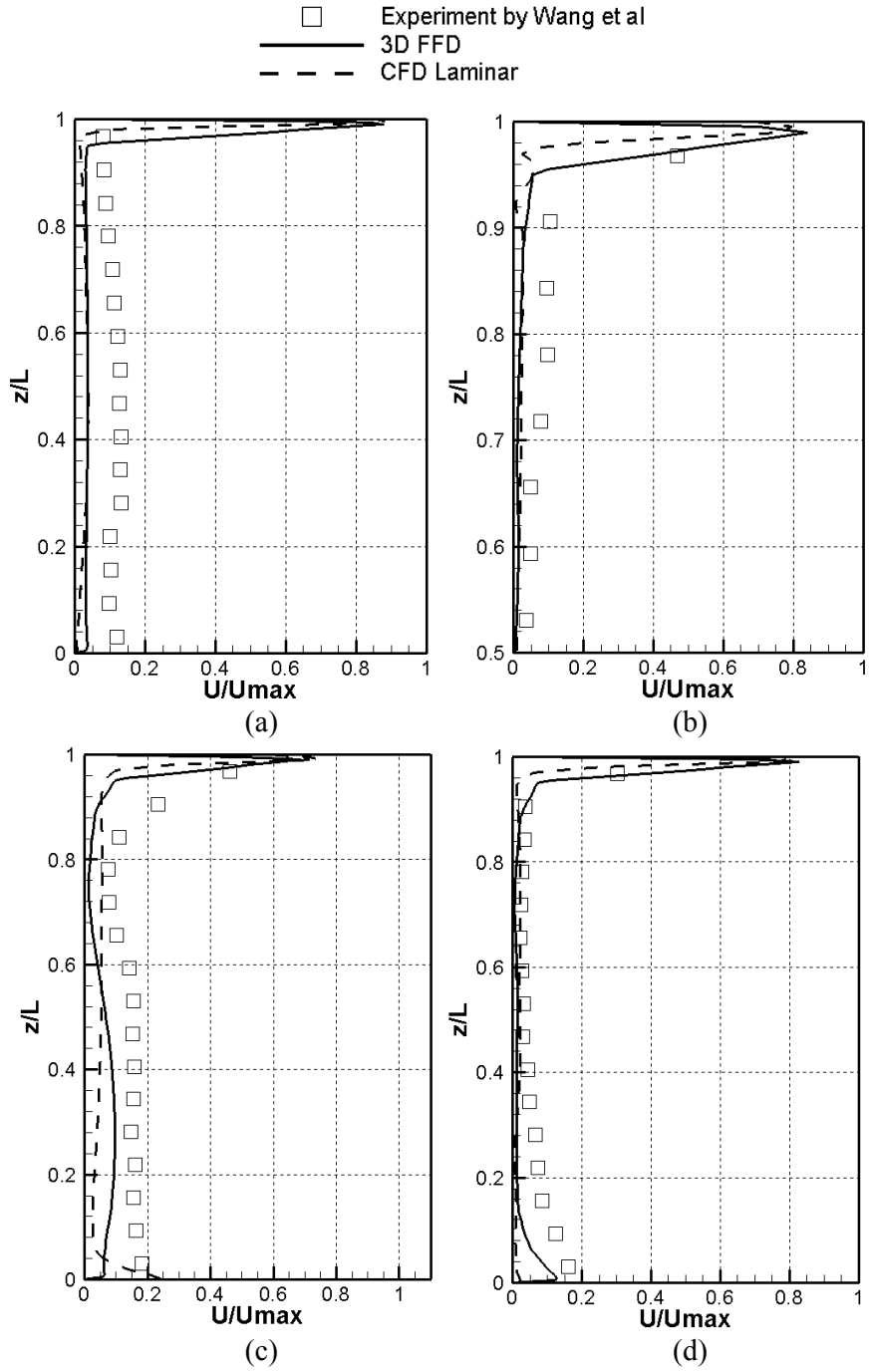

Figure 13

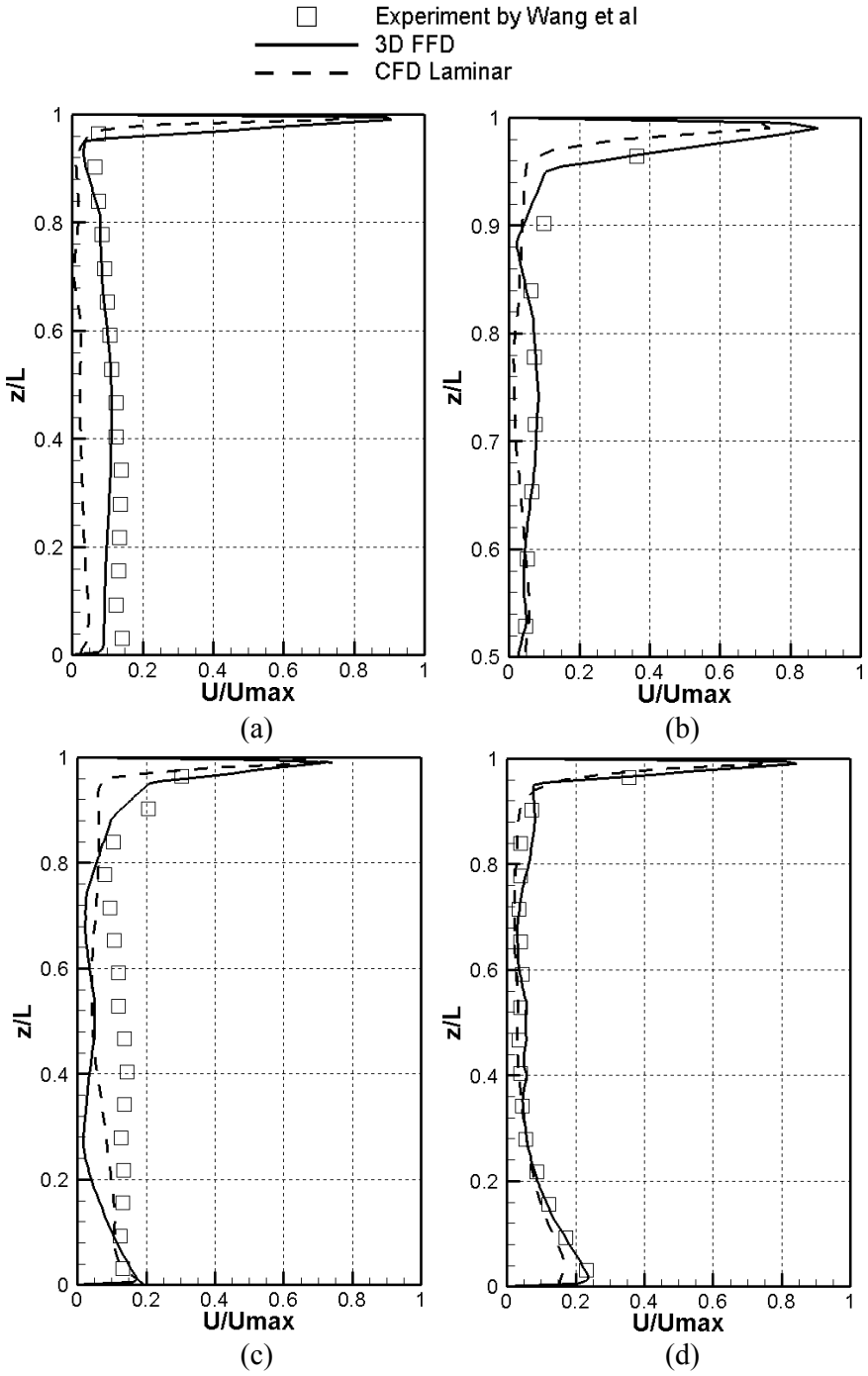

Figure 14

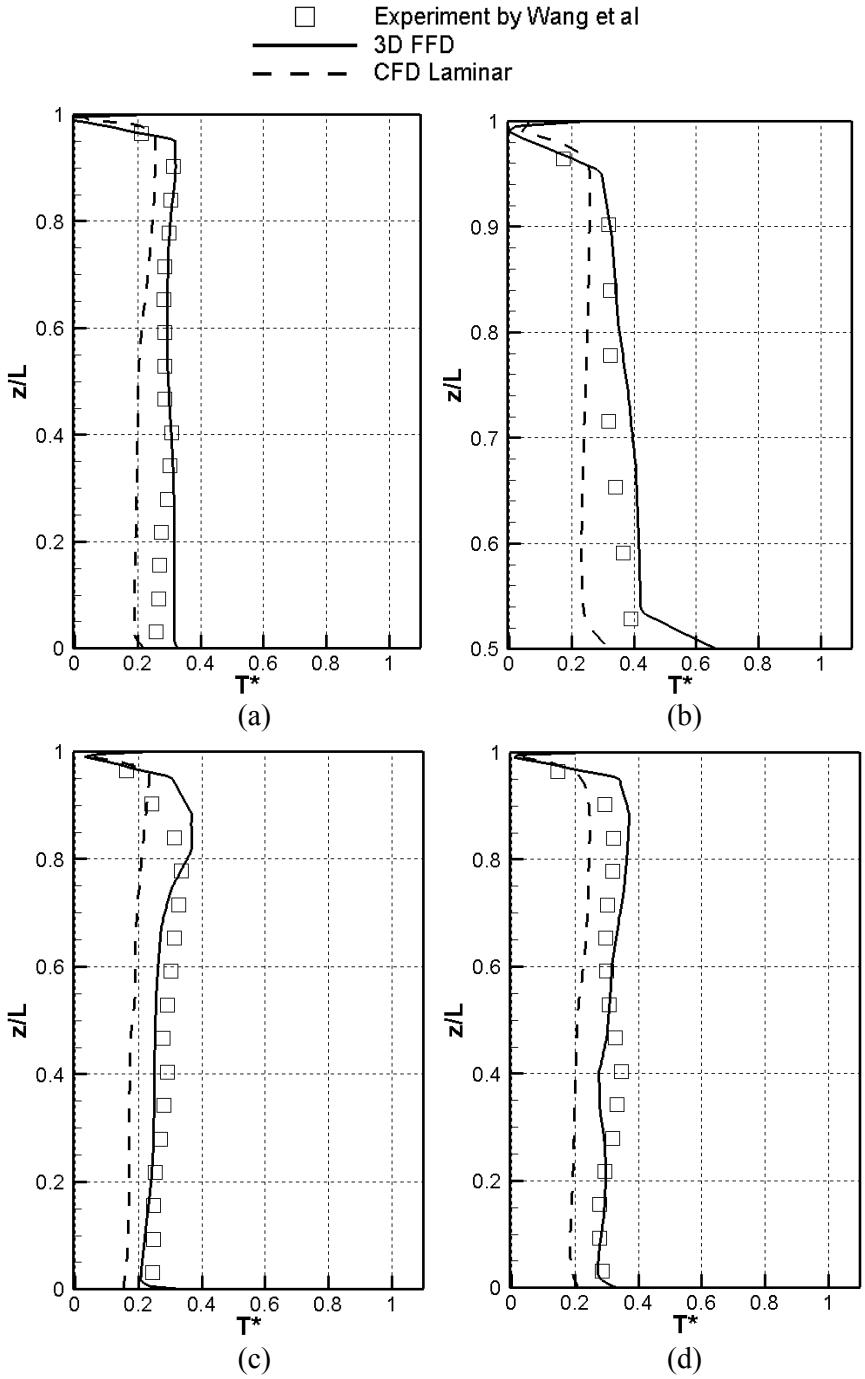

Figure 15